Design and Modeling of Waveguide-Coupled Single-Mode Microring Resonators

M. K. Chin, *Member, IEEE,* and S. T. Ho, *Member, IEEE*

Abstract—We discuss a first-order design tool for waveguide-coupled microring resonators based on an approximate solution of the wave propagation in a microring waveguide with micron-size radius of curvature and a large lateral index contrast. The model makes use of the conformal transformation method and a linear approximation of the refractive index profile, and takes into account the effect of waveguide thickness, dispersion, and diffraction. Based on this model, we develop general design rules for the major physical characteristics of a waveguide-coupled microring resonator, including the resonance wavelength, the free spectral range, the coupling ratio, the bending radiation loss and the substrate leakage loss. In addition, the physical model provides leads to alternative coupling designs. We present two examples, one using a phase-matching parallel waveguide with a smaller width than the ring waveguide, and the other using a vertical coupling structure. Both these designs significantly increase the coupling length and reduce or eliminate the dependence on a narrow air gap in a waveguide-coupled microring resonator.

Index Terms—Conformal transforms, microresonators, nanofabrication, nanophotonics.

I. INTRODUCTION

OPTICAL ring waveguide resonators are useful components for wavelength filtering, multiplexing, switching and modulation [1], [2]. The main performance characteristics of these resonators are the free-spectral range (FSR), the finesse (or Q-factor), the transmission at resonance, and the extinction ratio. The major physical characteristics underlying these performance criteria are the size of the ring, the propagation loss, and the input and output coupling ratios (equivalent to the reflectivities of a Fabry–Perot resonator). There are various components of losses, including sidewall scattering loss, bending radiation loss, and substrate leakage loss. Ring resonators based on (rib) waveguide structures with weak lateral confinement have very low sidewall scattering loss. However, the high radiative bending loss limits its minimum radius to about 2 mm, in which case the FSR will be small (in the order of 100 GHz [3]), and the finesse will also be low because the scattering loss is very high for such a large circumference, although the scattering loss per cm is lower. On the other hand, strongly guiding ring waveguides with very large lateral refractive index contrast (air-semiconductor-air) can have diameters as small as 1–2 μm with negligible
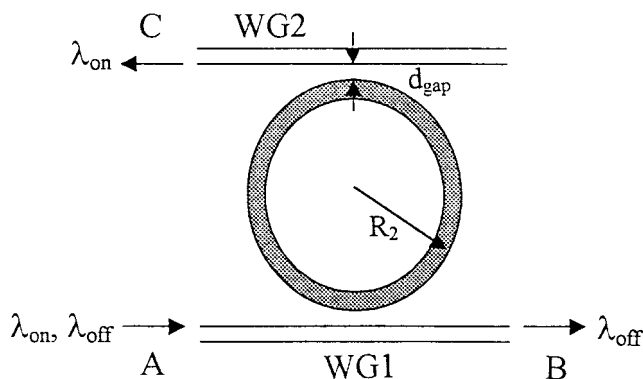
Fig. 1. A schematic of the waveguide-coupled microcavity resonator, showing a microring resonator coupled to straight waveguides.

bending loss. Therefore, compared with the weakly guiding waveguide, the strongly guiding microcavity can be up to 1000 times smaller. Because of the small size, the propagation loss in the cavity is also negligible. Consequently, both the FSR and the finesse are much larger for this resonator. An FSR of 6 THz (50 nm) can be achieved, sufficiently large to cover the entire 30-nm erbium amplifier bandwidth.

Fig. 1 shows a schematic of an add–drop filter (or optical switch) implemented with a microring resonator [4]. The two tangential straight waveguides (WG1 and WG2) serve as evanescent wave input and output couplers. If the signal entering port A is on-resonance with the ring or disk, then that signal couples into the cavity from WG1, couples out from the cavity into WG2, and exits the device at port C. A signal that is off-resonance with the cavity remains in WG1 and exits at port B. The critical dimension in this optical switch is the 0.1-μm gap separating the microring cavity from the tangential waveguides. These gap sizes determine the input and output coupling ratios of the resonator, which in turn determine the magnitude of the finesse and the at-resonance transmittance. In the case of a microring coupled to straight waveguides, the gaps are very small due to the strong optical confinement and the small coupling interaction length. These small gaps are difficult to fabricate. In particular, it is difficult to ensure that the two coupling gaps on both sides of the ring are identical. If the coupling factors are not equal, then the finesse and the ON–OFF ratio of the resonator will be reduced. To achieve more dependable performance, it is, therefore, useful to design alternative coupling structures that significantly reduce the dependence on a narrow air gap.

The aim of this paper is to model the wave propagation in a microring waveguide, to develop a first-order design tool that provides guidance for alternative coupling designs,

and to formulate general design rules for the major physical characteristics of a waveguide-coupled microring resonator. While there are available very precise numerical methods, such as the finite difference time domain (FDTD) method [5], that can solve the electromagnetic field distribution in any complicated three-dimensional (3-D) photonic structures, they are time consuming to use and, for most purposes, the accuracy is not essential for first-run designs. Recently, multiple coupled-resonator filters have also been proposed and modeled using the so-called "coupling of modes in time" method, in which the ring eigenmodes are never explicitly solved [6]. By contrast, we will follow the more conventional approach in which the waveguide eigenmodes are first solved, and then used to calculate the other parameters such as the coupling coefficient and radiation loss. This will be achieved using a model that is relatively simple and intuitive, approximate but reasonably accurate, and analytical wherever possible. The advantage of such an approach, as will be shown, is the gain in physical insight. Some approximations are necessary in order to simplify computations and the complexity associated with the 3-D nature of the problem. In particular, the treatment of the vertical dimension (thickness) of the device is approximate. Nevertheless, the model attempts to account for some of the 3-D physical effects such as waveguide dispersion, edge diffraction, and bending loss.

II. METHOD OF CALCULATION AND PHYSICAL CONSIDERATIONS

The current method is an extension of the conformal transformation method used previously for solving the waveguide modes of a microdisk structure [7]. This method is chosen because of the intuitive physical picture it gives, as will become apparent later. We consider a semiconductor waveguide with core thickness d, and core material index n_1, surrounded in the horizontal direction by air. The cladding material index is n_c, which for simplicity is assumed to be the same for both the upper and lower cladding layers. Two possible realizations for the vertical layer structure are shown in Fig. 2(a) and (b) where Fig. 2(a) is a weak vertical guiding structure with $n_c < n_1$. Since photons are strongly confined only in the horizontal direction, we call this the *Type I* or the *photonic well* structure. Fig. 2(b) is a strong vertical guiding structure where $n_c \ll n_1$. (For example, the low-index medium could be air, or acrylic/polyimide with $n_c \sim 1.5$.) Since the photons are strongly confined in both transverse dimensions we call this the *Type II* or the *photonic wire* structure. In theory the later structure is more interesting as photons are more strongly confined, but in practice it is not easy to realize, especially for electrically contacted devices.

A. Conformal Transformation Method for Ring Waveguides with Finite Thickness

In cylindrical coordinates, the ring waveguide mode may be given by the 3-D scalar wave equation

$$\frac{\partial^2 \varphi}{\partial r^2} + \frac{1}{r}\frac{\partial \varphi}{\partial r} + \frac{1}{r^2}\frac{\partial^2 \varphi}{\partial \phi^2} + \frac{\partial^2 \varphi}{\partial z^2} + k_1^2 \varphi = 0 \qquad (1)$$
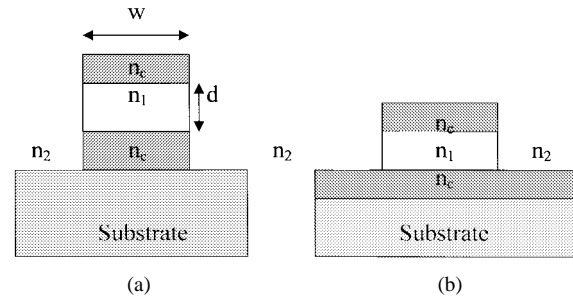

Fig. 2. Two possible realizations of the vertical layer structure: (a) Type I or weak vertical guiding structure and (b) Type II or strong vertical guiding structure. d is the waveguide core thickness and t_2 is the lower cladding or buffer thickness.

where $k_1^2 = k_o^2 n_1^2 = k_r^2 + \kappa_\phi^2 + k_z^2 = k_o^2(n_r^2 + n_\phi^2 + n_z^2)$, $k_o = 2\pi/\lambda$, and λ is the free space wavelength. For each k vector there are two modes corresponding to the two possible polarizations. These are the transverse electric (TE) and the transverse magnetic (TM) modes with the electric field and the magnetic field, respectively, parallel to the r direction. For simplicity we will consider only the TE mode, since the method of analysis is similar for the TM mode. For the TE mode, φ is the z component of the magnetic field (i.e., the electric field has no z component).

The conformal transformation to be discussed later applies only to the x-y plane. We, therefore, first reduce the 3-D waveguide problem to two-dimensional (2-D) by making two approximations. In the first approximation, we assume that the waveguide mode φ can be written in the form $\varphi = F(r, \phi)H(z)$, where $F(r, \phi)$ describes the mode in the x-y plane and $H(z)$ describes the resonant field in the z direction. In the second approximation, we use the effective index method (EIM) [8] to determine $H(z)$ and its associated wavevector component

$$k_z \equiv 2\pi n_z/\lambda. \qquad (2)$$

For verification of this approximation, we compare the effective indexes (n_{eff}) for both Type I and Type II waveguides calculated with EIM and with multigrid finite-difference numerical methods [9]. For example, the difference in (n_{eff}) between the two methods is shown for TM_{oo} mode in Fig. 3. Note that the EIM approximation is a good one except when the width is smaller than 0.2 μm for Type I waveguides and 0.4 μm for Type II waveguides.

Fig. 4(a) shows the approximate n_z for the TE modes as a function of the normalized core thickness, d/λ, for both Type I and Type II waveguides. In the Type I case we assume a GaAs core with $n_1 = 3.372$ and an $\text{Al}_{0.45}\text{Ga}_{0.55}\text{As}$ cladding with $n_c = 3.150$. Note that for Type II single-mode waveguides, d/λ should be <0.3, whereas d/λ could be much larger for Type I waveguides. Roughly speaking, $n_z < 1$ for Type I waveguides and $n_z > 1$ for Type II single-mode waveguides. For Type I waveguides, n_z depends also on the waveguide width, as shown in Fig. 4(b).

Having solved $H(z)$ and k_z, (1) can be reduced to the 2-D scalar wave equation for $F(r, \phi)$

$$\frac{\partial^2 F}{\partial r^2} + \frac{1}{r}\frac{\partial F}{\partial r} + \frac{1}{r^2}\frac{\partial^2 F}{\partial \phi^2} + q^2 F = 0 \qquad (3)$$
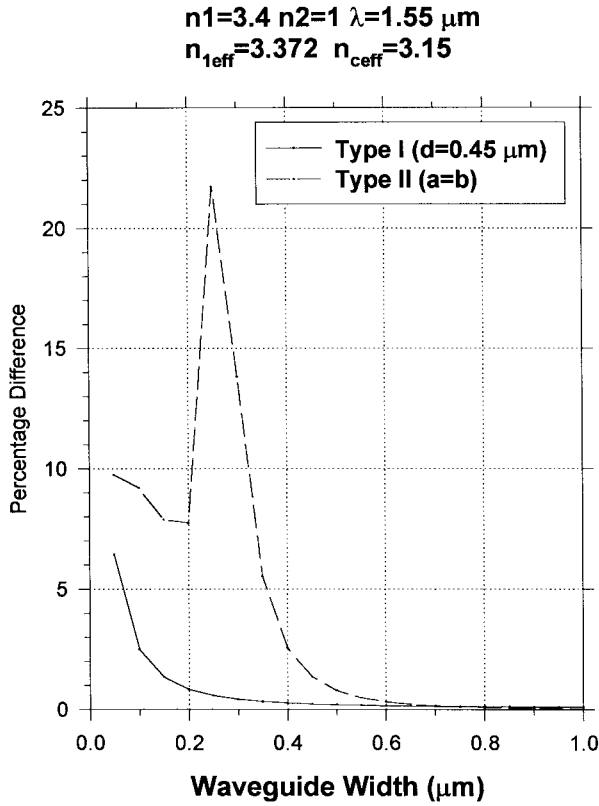
n1=3.4 n2=1 λ=1.55 μm
n_{1eff}=3.372 n_{ceff}=3.15

Fig. 3. Percentage error in effective index calculated by the effective index method and the finite-difference numerical method, for TM_{oo} mode in Type I and Type II waveguides as a function of waveguide width (a). The waveguide thickness (d) is assumed to be 0.45 μm for Type I waveguides. Type II waveguides are assumed to be square ($a = b$).

where $q^2(x,y) = k_1^2 - k_z^2$. We assume the ring to have a width of w, an inner rim radius of R_1, and an outer rim radius of R_2, as shown in Fig. 5(a). We next make a transformation to a new coordinate system u, v such that the curved waveguides become straight in the u–v plane. Such a transformation is given by [10]

$$u = R_{\text{eff}} \ln(r/R_{\text{eff}}), \quad v = R_{\text{eff}}\phi. \tag{4}$$

Our transformation is somewhat different from the literature in that we use R_{eff} instead of R_2 (or R_1), where R_{eff} is the effective ring radius to be defined later. The resulting wave equation in the (u, v) space is then

$$\frac{\partial^2 F}{\partial u^2} + \frac{\partial^2 F}{\partial v^2} + q^2 \exp(2u/R_{\text{eff}})F = 0 \tag{5}$$

where

$$q^2 = k_u^2 + k_v^2 = \begin{cases} k_1^2 - k_z^2 & \text{for } R_1 < r < R_2, \\ k_2^2 - k_z^2 & \text{for } r < R_1 \text{ and } r > R_2 \end{cases} \tag{6}$$

and $k_1 = 2\pi n_1/\lambda$, $k_2 = 2\pi n_2/\lambda$. The effect of waveguide thickness is now embedded in k_z. The transformed linear waveguide is shown in Fig. 5(b), with the straight edges at $u_1 = R_{\text{eff}} \ln(R_1/R_{\text{eff}})$ and $u_2 = R_{\text{eff}} \ln(R_2/R_{\text{eff}})$. The refractive index in this waveguide is a function of u, as illustrated in Fig. 6(a) for the two possible cases corresponding roughly to the Type I and Type II waveguides. In the former case, the effective refractive index outside the waveguide
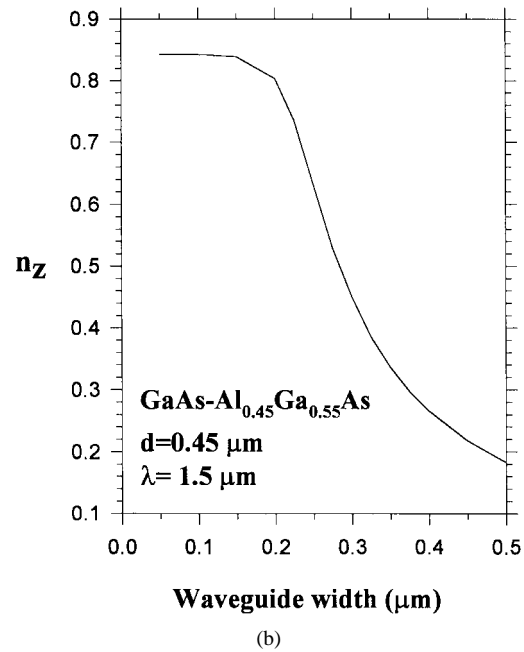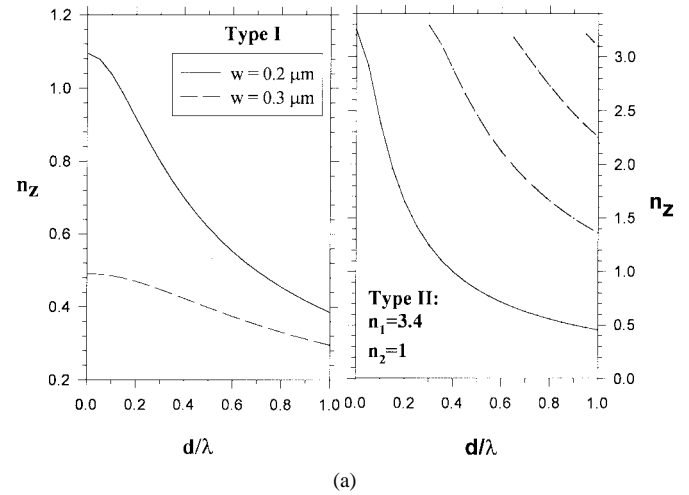

(a)

GaAs-$Al_{0.45}Ga_{0.55}$As
d=0.45 μm
λ= 1.5 μm

(b)

Fig. 4. (a) n_z, the equivalent index in the z direction for the TE modes, as a function of d/λ for Type I and Type II waveguides. (b) n_z as a function of waveguide width, for Type I waveguides with the given material compositions and core thickness.

increases radially as $e^{u/R_{\text{eff}}}$ so at some point the index will be large enough to support oscillatory modes. On the other hand, for Type II waveguides in which $k_z > k_2$, the field is completely evanescent outside the guide and there is no radiation loss.

B. The Effect of Diffraction

In reality, the evanescent tail of the bounded mode will diffract outside the waveguide. This means that k_z, which is continuous across the boundaries of the waveguide, must decrease monotonically once outside the waveguide since the field there is not guided. The dependence of k_z on u outside the waveguide corresponds to the diffraction effect. Here, we approximately include the effect by assuming that the evanescent wave outside the waveguide diffracts as a Gaussian wave, with the k_z value decreasing with r according to the
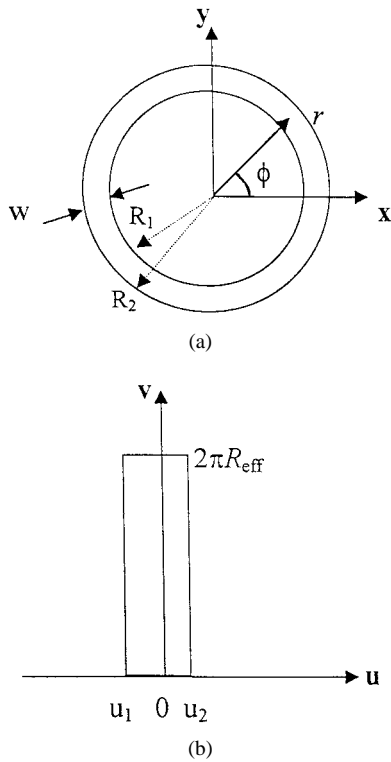
Fig. 5. (a) Geometry of the ring waveguide in the x-y plane. (b) Equivalent straight waveguide in the (u, v) transform space; u_1 and u_2 are the coordinates of the edges of the ring.

usual expression

$$k_{zo} = \frac{k_z}{\sqrt{1 + \left[\frac{\lambda|r - R_i|}{\pi \omega_o^2}\right]^2}}, \quad i = 1, 2 \tag{7}$$

where ω_o is the effective mode radius at the waveguide edge. This effective mode radius may be approximated by $\omega_o = d_{\text{eff}}/2$, where $d_{\text{eff}} = d + 2/\gamma_z$, γ_z being the decay constant of $H(z)$ outside the waveguide core. The diffraction effect changes the refractive index distribution outside the waveguide, as shown in Fig. 6(b). The change is especially drastic for the Type II case. In both cases, the external index for $u > u_2$ now increases monotonically with u and exceeds the waveguide effective index at some "turning" point u_o. Essentially, the effect of diffraction is to move this point closer to the waveguide edge. Beyond this point an oscillatory field exists meaning that there will always be some radiation loss through nonresonant tunneling.

Diffraction has two opposing effects on the field coupling between two adjacent waveguides. First, because $|k_2^2 - k_z^2|$ is reduced, the modal field will now decay less rapidly outside the ring waveguide, and therefore overlap more with the adjacent waveguide. Second, because the field expands in the vertical direction the coupling is reduced by the decreased modal overlap in the vertical (z) direction. Overall, the coupling may be diminished, especially for the Type II structures where the diffraction effect is strong. In other words, to achieve the same coupling coefficient in both Type I and Type II structures, the required gap spacing will have to be even smaller in the Type II structures, which aggravates the difficulty in realizing these

structures. For these reasons, we will henceforth focus mainly on the Type I structures.

C. The Physical Meaning of R_{eff}

We expect the radial distribution of the eigenmode in a curved waveguide to be somewhat skewed toward the outer edge (u_2). Different parts of the radial wavefunction will propagate in the ϕ (or v) direction with slightly different pathlengths given by $r\phi$. Therefore, for the radial mode as a whole to remain in phase, the propagation constant must vary along u. This shows that in a curved waveguide the u and v components are inherently coupled, and the eigenmodes, in general, cannot be separated neatly into u and v components. Nevertheless, to make the solution tractable, we shall assume the separation of variables and write

$$F(u, v) = \tilde{F}(u) \exp(ik_v v). \tag{8}$$

In other words, we assume that the *centroid* of the radial intensity distribution, $|\tilde{F}(u)|^2$, propagates around the ring with an *average* propagation vector k_v. R_{eff} is then the *effective* ring radius, defined as the radial distance to the *centroid* of the radial function [11]. The resonance condition in the propagation direction requires that $k_v R_{\text{eff}} = m$, where m is an integer called the azimuthal mode number, which gives the number of nodes along the ϕ direction. Clearly, k_v and R_{eff} are inter-dependent and must be solved self-consistently, along with the radial function $F(u)$, which is now given by the one-dimensional (1-D) wave equation

$$\frac{d^2 \tilde{F}}{du^2} = -k_u^2(u)\tilde{F} \tag{9}$$

where $k_u^2 = (k_i^2 - k_z^2)\exp(2u/R_{\text{eff}}) - k_v^2$ ($i = 1, 2$ as before). This equation has a discrete set of solutions which are characterized by a radial mode number, l, giving the number of nodes in the r direction. Once k_v and R_{eff} are known, the resonance wavelength of the cavity is given by

$$\lambda_{ml} = \frac{2\pi n_v R_{\text{eff}}}{m} \tag{10}$$

where n_v, defined by $k_v = 2\pi n_v/\lambda$, is implicitly dependent on l. The resonance frequency is then given by $v_{ml} = c/\lambda_{ml}$, and the FSR is given by $\Delta\lambda_{\text{FSR}} = 2\pi R_{\text{eff}}[\frac{n_v(\lambda_m)}{m} - \frac{n_v(\lambda_{m+1})}{m+1}]$. The dependence of n_v on wavelength is known as the waveguide dispersion.

D. Solution for the Radial Modes

Equation (9) is similar to the Schrodinger equation of quantum mechanics, with k_v^2 corresponding to the "energy" eigenvalue and $(k_i^2 - k_z^2)\exp(2u/R_{\text{eff}})$ to the "potential." The problem of wave propagation (eigenfunctions) in a waveguide (quantum well) with arbitrary refractive index (potential) profile can be solved by the transfer matrix method [12] or the WKB method [13]. Here, we aim for a simpler solution, which is based on the observation that the index profiles in Fig. 6(a) and (b) are approximately linear inside the waveguide, and also over most regions of interest outside the waveguide where the field is not negligibly small. This linear approximation of the index profile is good for strongly confined, single-mode waveguides, except when the radii of curvature are very small
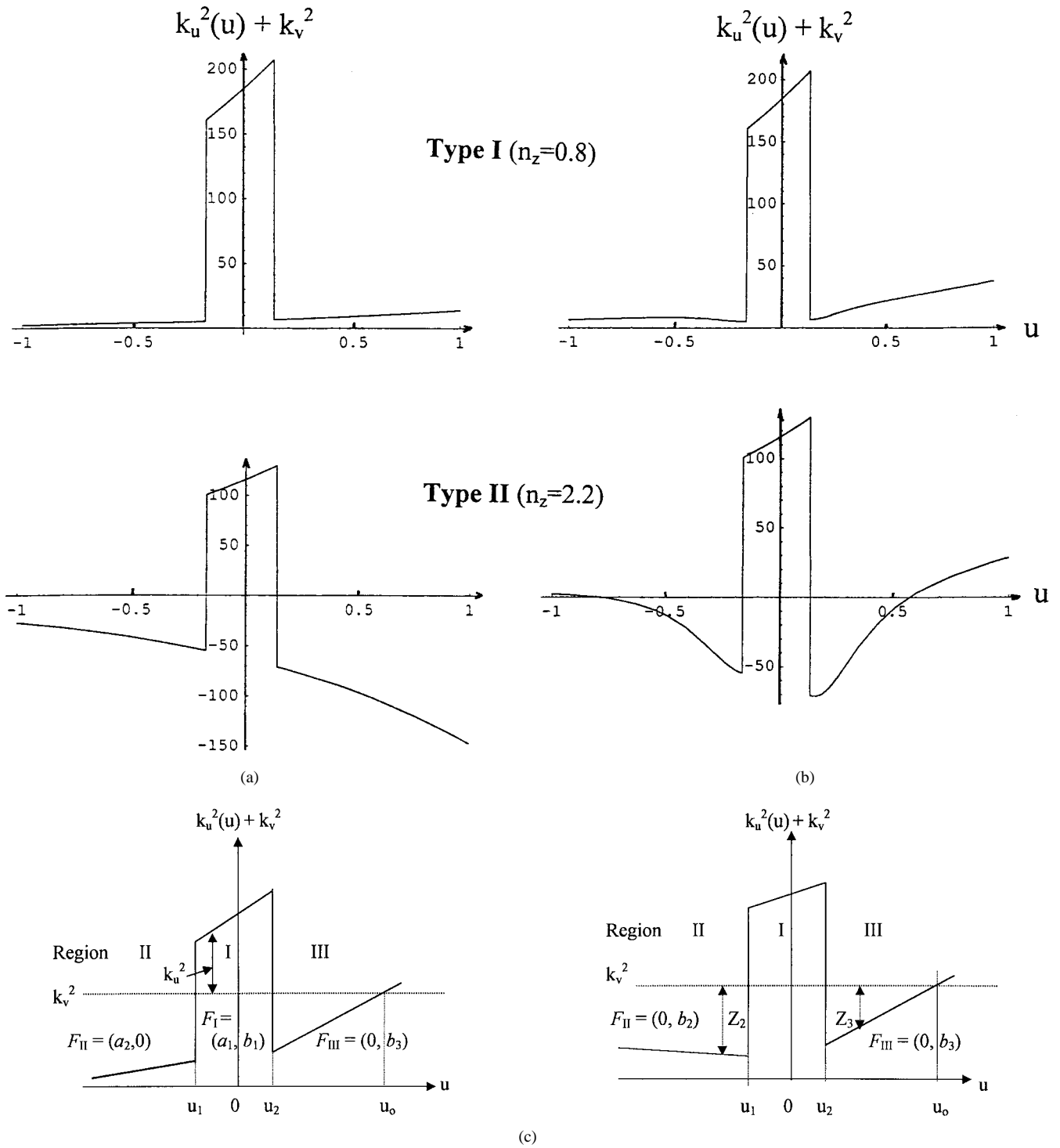
Fig. 6. Plots of the "potential" $k_u(u)^2 + k_v^2$ as a function of u for Type I and Type II waveguides: (a) without considering the diffraction effect and (b) with diffraction taken into account. (c) Linear approximations of the "potential" (with diffraction included) in various regions, showing the two possible cases where the potentials in Region II have opposite slopes, resulting in different solutions (F_{II}) in that region. Various notations used in the text are indicated.

($R_2 < 1$ μm). Within this linear approximation, (9) can be solved analytically in terms of Airy functions, much like the analogous problem of a quantum well in the presence of an applied electric field [14]. The same technique has also been applied by Goyal *et al.* to bent planar waveguides [15]. We briefly describe the method below.

Consider Region I as shown in Fig. 6(c). In the linear approximation, we write $(k_i^2 - k_z^2) \exp(2u/R_{\mathrm{eff}}) \sim c_1 + d_1 u$,

where c_1 and d_1 are constants to be determined case by case. Equation (9) becomes

$$\frac{d^2 \tilde{F}}{du^2} = -[c_1 + d_1 u - e]\tilde{F} \tag{11}$$

where $e = k_v^2$ is the eigenvalue. It can be shown that, by defining the dimensionless variable $Z_1 = -(c_1 + d_1 u - e)/l_1$

where $l_1 = d_1^{2/3}$, (11) is reduced to the Airy equation

$$\frac{d^2\tilde{F}}{dZ_1^2} = -Z_1\tilde{F}(Z_I) \tag{12}$$

the general solution for which is a linear combination of Airy functions

$$F(Z_I) = a_1 Ai(Z_I) + b_1 Bi(Z_I). \tag{13}$$

Similar parameters c, d, and Z can be defined for Regions II and III, where the Airy solutions are labeled by (a_2, b_2) and (a_3, b_3), respectively. The coefficients a's and b's are then found by matching boundary conditions at the two interfaces Z_{12} (corresponding to $u = u_1$) and $Z_{13}(u = u_2)$. The boundary conditions refer to the continuities of F and $dF/du = (d_i/l_i)dF/dZ_i(i = 1, 2, 3)$. The final result can be expressed as a matrix equation relating the field amplitudes on both sides of the waveguide

$$\begin{bmatrix} a_3 \\ b_3 \end{bmatrix} = \begin{bmatrix} M_{11} & M_{12} \\ M_{21} & M_{22} \end{bmatrix} \begin{bmatrix} a_2 \\ b_2 \end{bmatrix}. \tag{14}$$

The eigenvalue equations are then determined by the physical requirement that the wavefunctions decay away from the waveguide. This leads to two distinct cases, with different eigenvalue equations.

Case i: As shown in part (i) of Fig. 6(c), the behavior of the Airy functions dictates that $b_2 = a_3 = 0$, and the eigenvalue equation is

$$M_{11} = 0 \tag{15}$$

where

$$M_{11} = \frac{1}{D}\{[Ai(Z_{13})Bi'(Z_3) - Ai'(Z_{13})Bi(Z_3)]$$
$$\times [Ai(Z_2)Bi'(Z_{12}) - Ai'(Z_2)Bi(Z_{12})]$$
$$+ [Bi(Z_{13})Bi'(Z_3) - Bi'(Z_{13})Bi(Z_3)]$$
$$\times [Ai'(Z_2)Ai(Z_{12}) - Ai(Z_2)Ai'(Z_{12})]\}.$$

Case ii: As shown in part (ii) of Fig. 6(c), in this case $a_2 = a_3 = 0$, and the eigenvalue equation is

$$M_{12} = 0 \tag{16}$$

where

$$M_{12} = \frac{1}{D}\{[Ai(Z_{13})Bi'(Z_3) - Ai'(Z_{13})Bi(Z_3)]$$
$$\times [Bi(Z_2)Bi'(Z_{12}) - Bi'(Z_2)Bi(Z_{12})]$$
$$+ [Bi(Z_{13})Bi'(Z_3) - Bi'(Z_{13})Bi(Z_3)]$$
$$\times [Bi'(Z_2)Ai(Z_{12}) - Bi(Z_2)Ai'(Z_{12})]\}.$$

The primes in these equations denote first derivatives of the Airy functions with respect to u. Although strictly speaking the eigenstates are not bound, the decay time of these states are so long that they can be considered as quasistationary states.

III. RESULTS AND DISCUSSIONS

A. Effective Indexes and Radial Wavefunctions

The solutions to (15) or (16) yield the eigen-indexes (n_v) and eigenfunctions of all the ring waveguide modes. The effective index n_v in a microring waveguide is a function of the radius (say, R_2), the waveguide width (w), the vertical waveguide structure (d, n_1, n_c), and the optical wavelength (λ). The dependence on the vertical waveguide structure is lumped into a single parameter n_z as discussed before. In most cases, we are interested in waveguides that have a single transverse mode.

Fig. 7(a)–(c) shows the changes of n_v for TE modes as the waveguide parameters n_z, R_2, and w, respectively, are varied while the others are kept constant. One can see that n_v changes significantly only if the rings are small, and that w is typically less than 0.3 μm for single-transverse-mode waveguides at $\lambda = 1.55$ μm. As the width increases, many more radial modes can exist, each having a different n_v curve.

To illustrate the radial eigenfunctions Fig. 8 shows the intensity profiles $|F_l(r)|^2$ of the four radial modes $(l = 0, 1, 2, 3)$ supported in a microring waveguide with a width of 0.9 μm and a radius of 3 μm. The indicated values of R_{eff} give the positions of the "center of gravity" of these modes. Let us consider first the high-order modes. These modes tend to be more concentrated near the inner edge of the waveguide, implying that the radial propagation of these modes is slower near the inner edge. This fact can be deduced from Fig. 6(c), which shows that k_u^2 decreases as the inner edge u_1 is approached. Next, we consider the low-order modes such as F_o and F_1. The centroids of these modes are shifted toward the outer edge of the waveguide, as shown by the fact that $R_{\mathrm{eff}} > (R_1 + R_2)/2 = 2.55$ μm. In fact, F_o changes slowly to a microdisk-like *whispering gallery* mode as the waveguide width is increased. The transition from microring mode to microdisk mode is illustrated in Fig. 9, which depicts the normalized intensity profile of F_o as the width of the waveguide is increased. Note that F_o hardly touches the inner rim, and its position and profile remain unchanged, as long as $w > 0.6$ μm. As the width is increased, the effective index (k_v^2) increases and moves up into the triangular region of the "potential" inside the waveguide [see insets]. Once k_v^2 is inside the triangular region, the eigenmode sees a potential similar to that in a microdisk, and therefore is guided in the same way.

B. Resonance Wavelength and Free Spectral Range

Nanoscale waveguides display significant dispersion and because the resonance modes for the small ring waveguides are spaced far apart, the effective index will be different at each resonance wavelength. Over a small wavelength range, the material index dispersion may be neglected in the calculation of n_v. A typical result around $\lambda = 1.55$ μm is shown in Fig. 10(a). It shows that n_v is essentially a linear, decreasing function of the wavelength, with a slope dependent somewhat on the width w. Using these linear functions, λ can be determined in terms of the azimuthal mode number m for given n_z, w and R_2, according to (10). These are shown in Fig. 10(b) where several important results can be noted. First, for a fixed R_2, as the waveguide width decreases, each resonance is shifted toward shorter wavelength or higher frequency. Secondly, the wavelength decreases with the mode number, and the wavelength spacing, or FSR, decreases as the wavelength decreases. This behavior agrees with experimental observations [4].
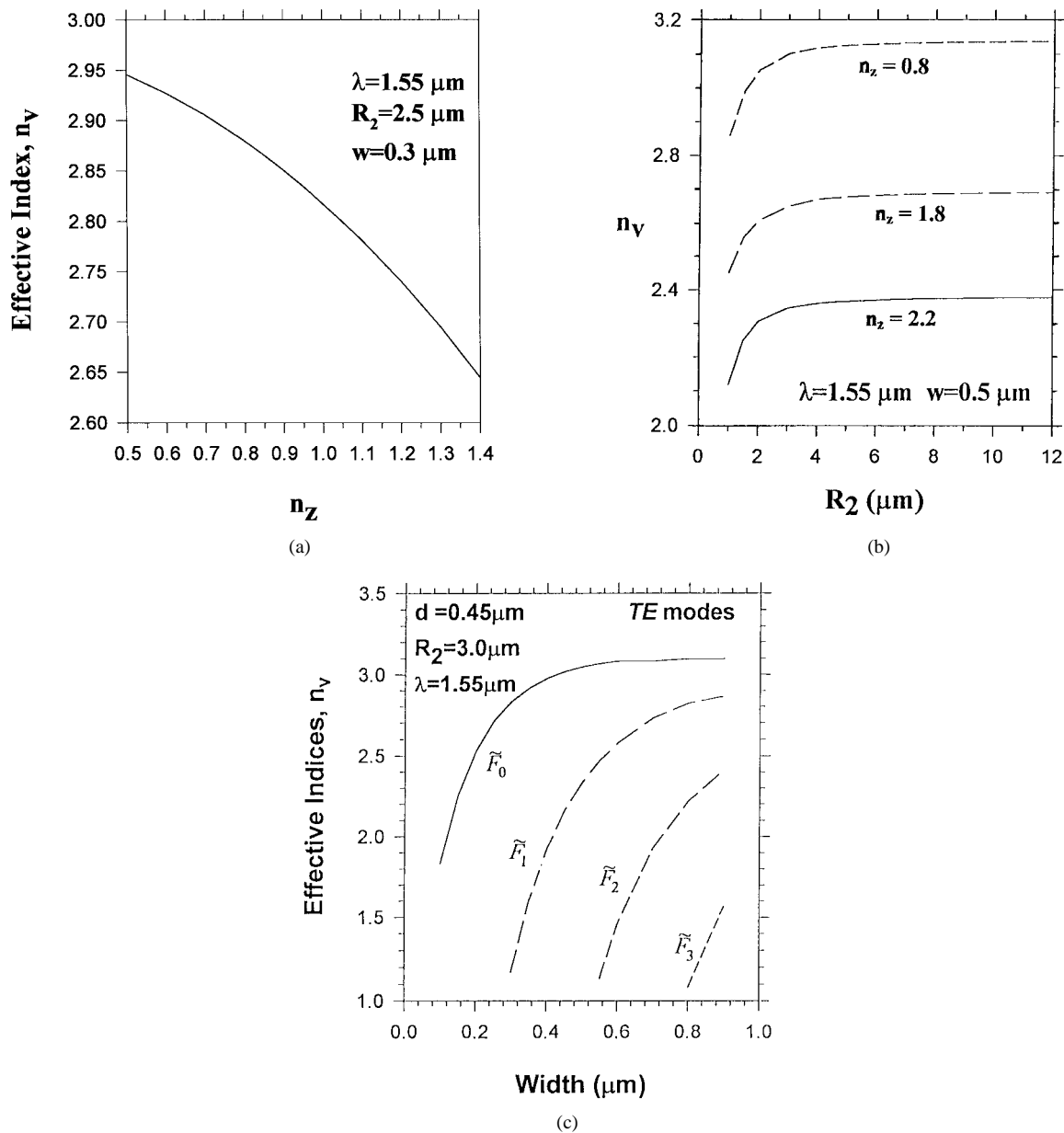
Fig. 7. While keeping the other parameters constant, these figures show how the effective index n_v depends on (a) n_z, which is linked to the waveguide thickness (d) through Fig. 4, (b) the ring radius R_2 (for various n_z), and (c) the waveguide width w, showing how n_v varies with the radial wavefunctions.

In Table I, the wavelengths and the FSR for major resonances around 1.55 μm in a ring resonator with the parameters $w = 0.3$ μm, $R_2 = 2.5$ μm, and $d = 0.45$ μm, are listed and compared with those calculated using the FDTD numerical simulations [5]. The good agreement between the two sets of results gives us confidence that our method is reasonably accurate. For the 5-μm diameter resonators, we note that the FSR can be as large as 50 nm (6 THz), sufficient to cover the entire 30-nm Erbium amplifier bandwidth. The extremely large FSR represents one of the advantages of nano-photonic semiconductor microcavity resonators.

C. Resonant Waveguide Coupling and Coupling Factor

In a waveguide-coupled microring resonator, the coupling gap size is determined by the amount of coupling required

and the coupling length available. A larger gap is desirable as it increases the fabrication tolerance. For a given coupling coefficient, the gap size can be enlarged if the coupling distance is increased. The coupling distance can be increased by using several configurations. A vertical resonant coupling configuration is discussed in Section III-F. Two *planar* configurations, as shown in Fig. 11, are discussed here. The more obvious one is the "racetrack" configuration, where the coupling distance is approximately the length of the straight sections, which are tangential to the semicircular arcs at both ends. At the transitions between the curved and the straight sections, the mode will change adiabatically between the radial mode in a curved waveguide and the normal mode in a straight waveguide. As the straight sections are lengthened the radius of the curved sections must be reduced if the total cavity length is to remain constant.
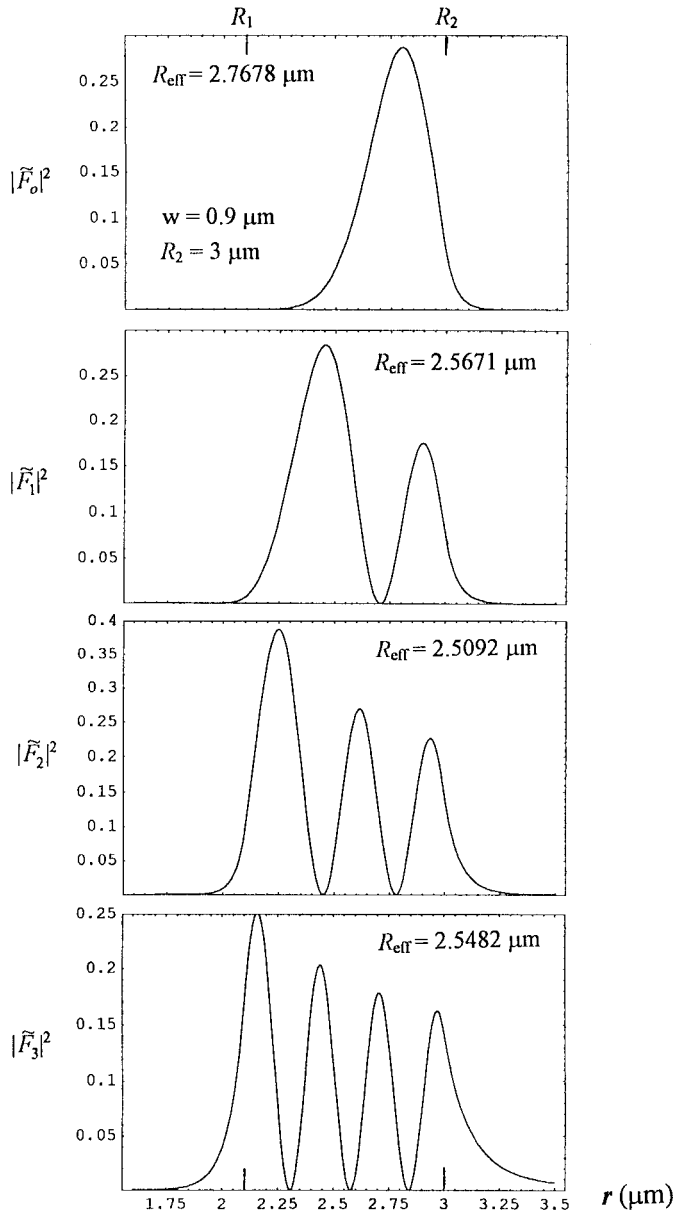
Fig. 8. Intensity profiles (in real space) of the four radial modes supported in a microring waveguide with a width of 0.9 μm and a radius of 3 μm. The R_{eff} values give the positions of the centroids of these modes.

Fig. 9. Normalized intensity profile of the lowest order radial mode in a microring as the width of the waveguide is increased from 0.15 μm to 1.5 μm. The two insets show the "potential" profiles and positions of the effective index eigenvalues (k_v^2) when $w = 0.3$ μm and $w = 0.6$ μm, respectively.

Fig. 11(b) shows the alternative configuration where the microring is coupled to a parallel curved waveguide over a significant part of the circumference. Note that the physical pathlengths in the concentric coupled sections in the two waveguides are different. In other words, if the coupled waveguides are identical, the propagating wavefronts in the two waveguides will in general be out of phase by $(n_{v2}R_{\text{eff}2} - n_{v1}R_{\text{eff}1})\phi$ after traveling an angle of ϕ. Therefore, to maintain phase matching, the two waveguides must be *different* in such a way that $n_{v1}R_{\text{eff}1} = n_{v2}R_{\text{eff}2}$. This can be achieved by varying the width of the outer waveguide. Fig. 12(a) shows the product $n_v R_{\text{eff}}$ as a function of w, for two concentric waveguides spaced 0.3 μm apart. We see that it is possible to match the optical pathlengths by choosing a suitable combination (w_1, w_2) for the two waveguides, such as $(0.4~\mu$m,
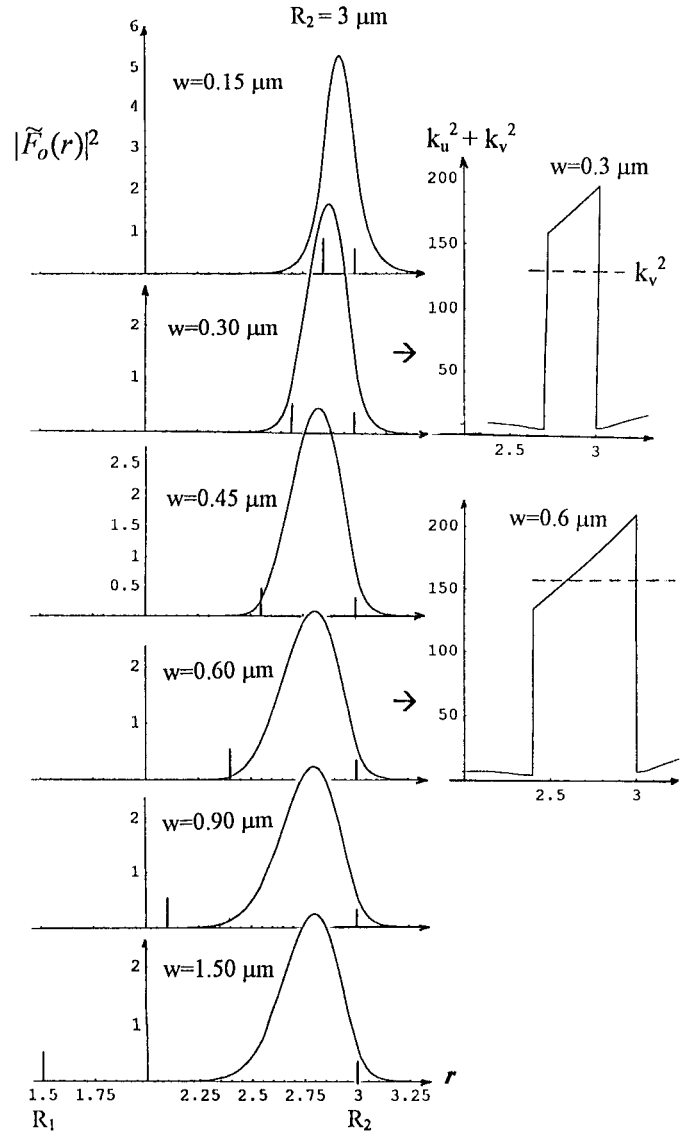
0.2 μm) in the case shown. The matching combinations of (w_1, w_2) are displayed in Fig. 12(b) for two cases of different radii and gap spacings. Note that the inner waveguide, which is required to have a larger value of n_v, will always be wider than the outer waveguide because n_v is an increasing function of w [see Fig. 7(c)].

The coupling coefficient (K) between two parallel waveguides, in the weak coupling limit applicable in most cases, is given by [16]

$$K = \frac{\omega}{4} \frac{\langle 1|\Delta\varepsilon|2\rangle}{\sqrt{\langle 1|1\rangle\langle 2|2\rangle}} = \frac{\omega^2}{2} \frac{\mu}{\sqrt{k_{v1}k_{v2}}} \langle 1|\Delta\varepsilon|2\rangle = \frac{\langle 1|\Delta q^2|2\rangle}{2\sqrt{k_{v1}k_{v2}}}$$

(17)

where $<1|$ and $<2|$ denote the radial modes in waveguide 1 and 2, respectively, k_{v1} and k_{v1} are their propagation vectors, $\Delta\varepsilon$ is the dielectric perturbation and Δq^2 is the perturbation in q^2 [cf., (3)] due to the presence of the other waveguide. In the
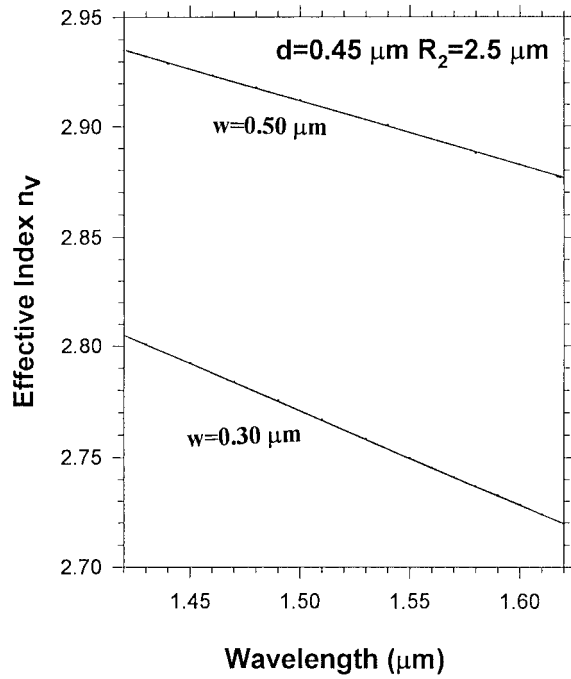
(a)
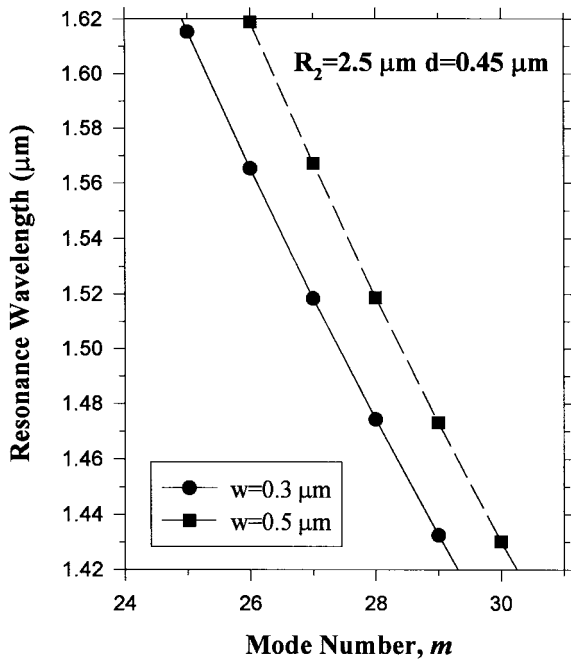
(b)

Fig. 10. (a) Effective index of the microring waveguide as a function of wavelength (in the vicinity of 1.5 μm) for two different waveguide widths. (b) The resonance wavelengths and the corresponding azimuthal mode numbers (m).

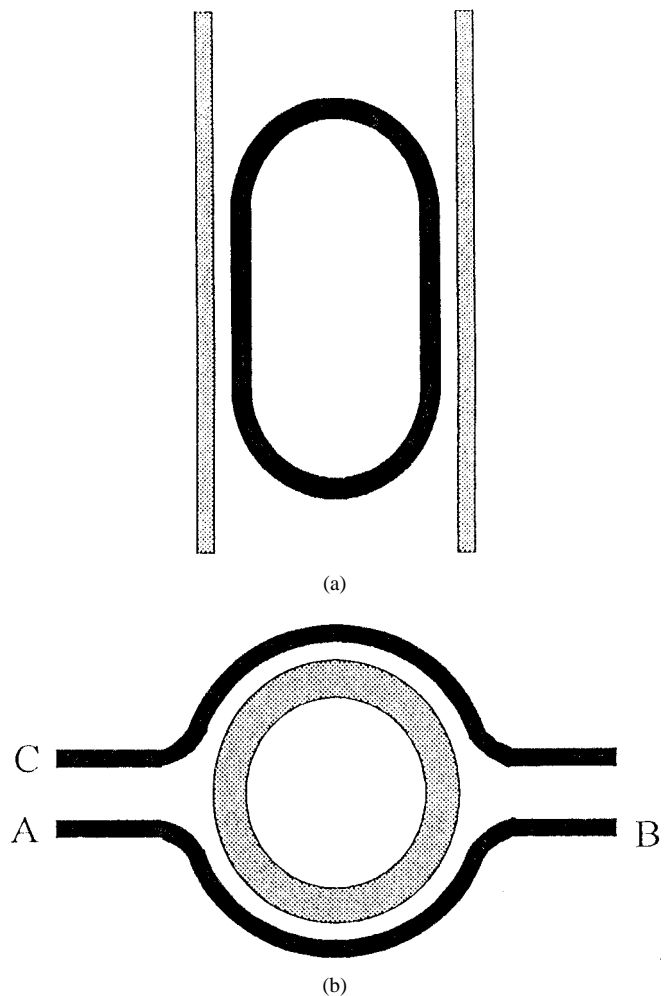|	This method		FDTD method	
m	λ_m (nm)	FSR (nm)	λ_m (nm)	FSR (nm)
25	1615.27		1613.10	
		49.96		50.66
26	1565.31		1562.44	
		49.96		47.56
27	1518.35		1514.88	
		44.23		44.73
28	1474.12		1470.15	
		41.72		42.17
29	1432.30		1427.98	

(a)

(b)

Fig. 11. Two *planar* geometries for resonant coupling that may give a larger coupling length: (a) the "race-track" configuration and (b) a microring coupled to parallel curved waveguides. Notice the outer waveguide is narrower than the inner waveguide.

case of resonant coupling, since the coupled eigenmodes in the concentric ring waveguides are moving in phase, the coupling coefficient between them can be calculated in exactly the same way as for parallel straight waveguides. (The ring nature of the waveguides is built into the radial wavefunctions.)

The coupling coefficients are a function of wavelength. The results for $\lambda = 1.55$ μm are shown in Fig. 13 as a function of gap spacing. Note that as the gap spacing is changed, the width

of the outer waveguide has to be modified somewhat in order to maintain phase matching with the inner waveguide (w_1 is assumed fixed). Once K is determined, the coupling factor P_c, or the fractional power coupled from one waveguide to another after a length l, is given by $\sin^2(Kl)$. Fig. 14 gives P_c, in the weak coupling limit, for various coupling lengths
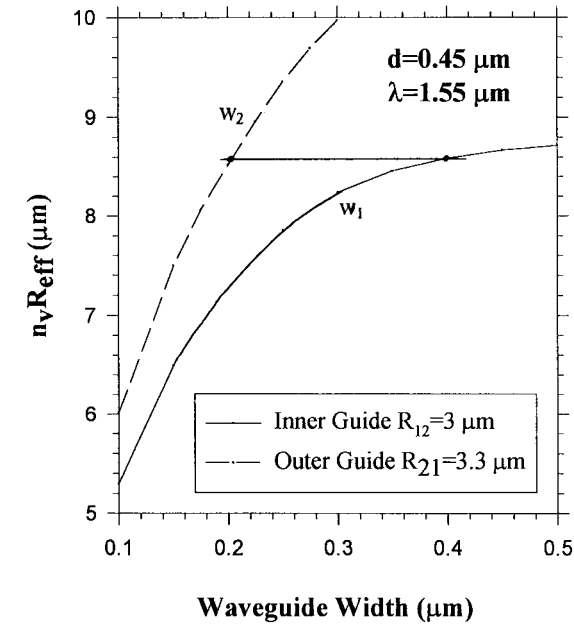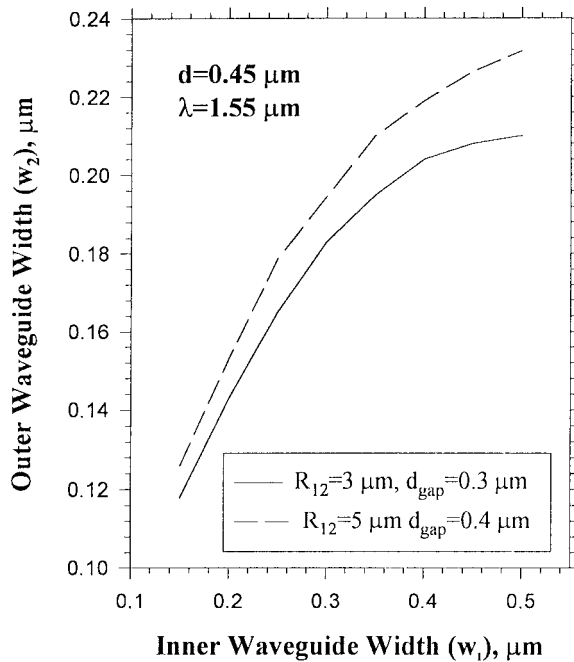
Fig. 12. (a) The optical pathlength (the product of n_v and R_{eff}) in two concentric ring waveguides, separated by a 0.4-μm wide gap, as a function of their waveguide widths. The inner ring has an outer radius (R_{12}) of 5 μm, while the outer ring has an inner radius (R_{21}) of 5.4 μm. The phase-matched pair (w_1, w_2) is joined by a horizontal line. (b) Matching combinations of w_1 and w_2 for two cases with different values of radius and gap spacing.

and gap sizes. It can be used to design the gap size and coupling length required to achieve a desired coupling factor. The coupling factor should be larger than the scattering loss per round trip, which is typically 1–2%. In the parallel coupling scheme, the coupling length is typically limited to a quadrant, so $l \sim \pi R_{\text{eff1}}/2 < 5$ μm (for $R_{\text{eff1}} \sim 3$ μm). With this coupling length, a coupling factor of 1–2% can be achieved with a coupling gap between 0.3 and 0.4 μm, or 3–4 times
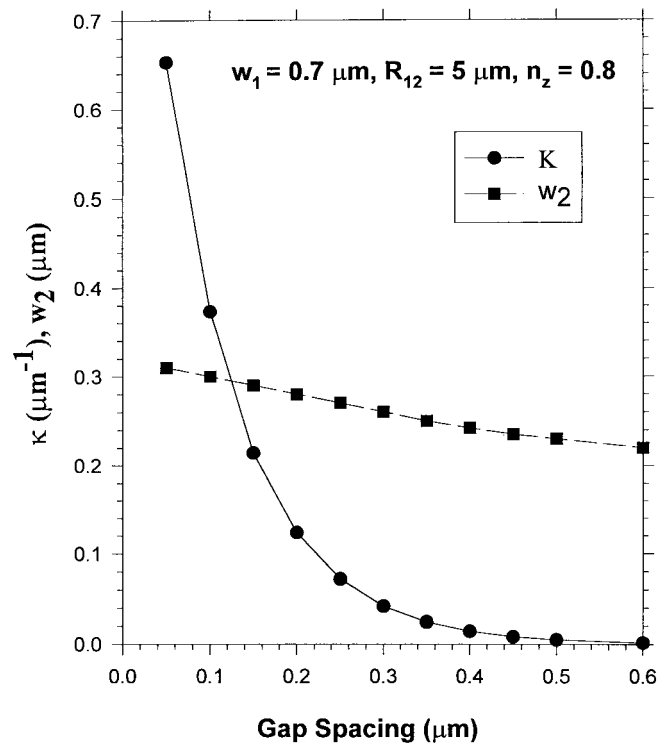

Fig. 13. The coupling coefficient (in μm^{-1}) between two resonant concentric ring waveguides as a function of their gap spacing, and the corresponding width (w_2) required of the outer waveguide in order to maintain phase-matching. The inner waveguide has a fixed width (w_1) and radius (R_{12}).

wider than the 0.1-μm gap currently used in the tangential waveguide structure [4]. Although the fabrication tolerance for the 0.3-μm gap is still small, it is not as stringent as for the 0.1-μm case. For larger microring resonators, the gap will be even larger and the coupling coefficient will be much less sensitive to small variations in the gap size.

D. Radiation Loss

The radial field decays as it exits the ring edge until the outer index grows exponentially and becomes greater than the azimuthal index $n_v(u)$. At this point, $k_u(u)$ becomes real, and the field begins to propagate once again. This propagation of the radial field is a nonresonant coupling of the field to the outer high-index region and constitutes the radiative bending loss. The value of the field intensity at this point where the decaying field begins to propagate is analogous to solving for the tunneling of light through a lossy barrier, and can be calculated in a similar fashion to the quantum mechanical tunneling (such as the alpha-particle emission from a nucleus). In the WKB approximation, the transmission coefficient (T) through the barrier (the region from u_2 to u_o) is given by [17]

$$T = \exp\left(-2 \int_{u_2}^{u_o} \kappa_u \, du\right) \qquad (18)$$

where

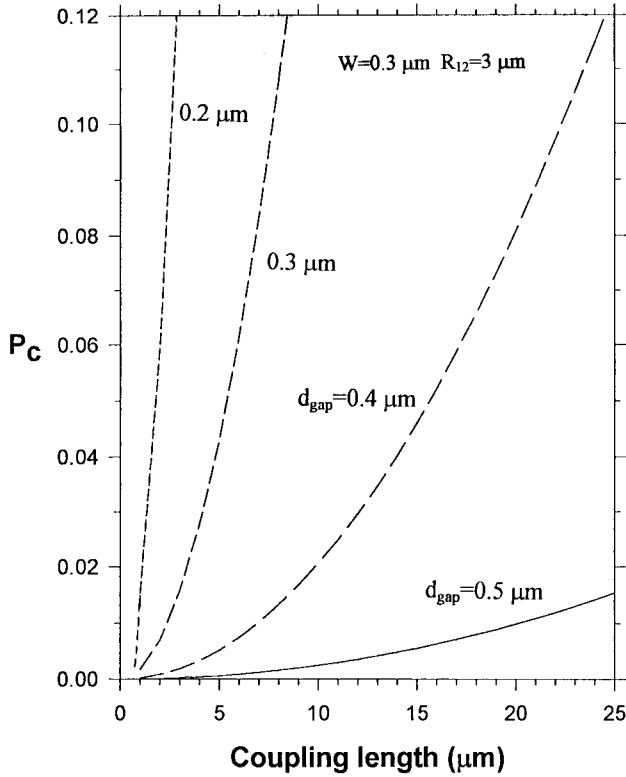$$\kappa_u(u) = \sqrt{k_v^2 - \left(k_2^2 - k_z^2(u)\right)\exp(2u/R_{\text{eff}})} \qquad (19)$$

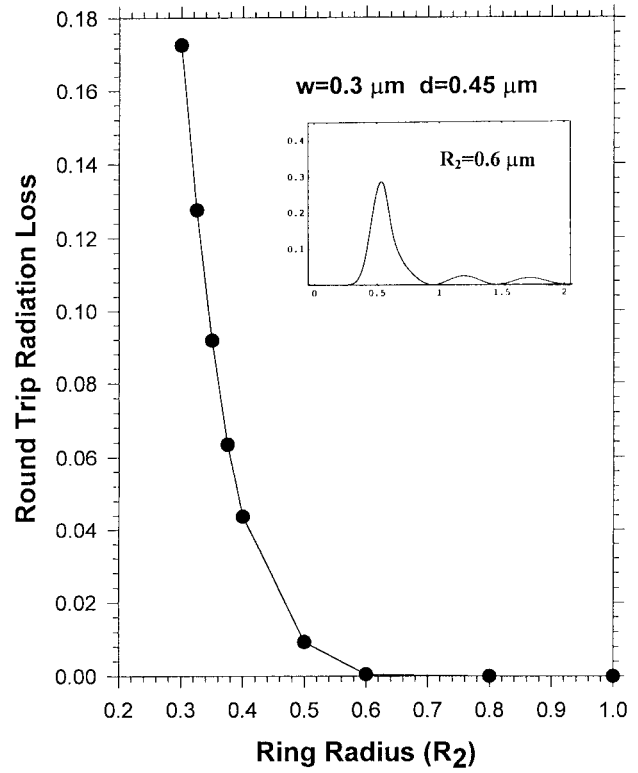Fig. 14. A plot of coupling factor (P_c) as a function of coupling length for various gap sizes.

Fig. 15. The round-trip radiation loss as a function of the ring radius. The inset is a plot of the radial wavefunction for the case $R_2 = 0.6$ μm. The radiation loss is less than 1% for diameters greater than 1 μm.

is the radial field decay factor outside the waveguide. The turning point u_o is given by $\kappa_u(u_o) = 0$ [see Fig. 6(c)], or $u_o = (R_{\mathrm{eff}}/2)\ln[k_v^2/(k_2^2 - k_z^2)] = (R_{\mathrm{eff}}/2)\ln[n_v^2/(n_2^2 - n_z^2)]$, which is an implicit equation for u since k_z is a function of u as in (7).

To calculate the round-trip radiation loss, we note that in making one round-trip, the waveguide mode makes a number of bounces in the radial direction equal to the azimuthal mode number, $m = 2\pi R_{\mathrm{eff}}/(\lambda_o/n_v)$. Thus the round trip loss is mT, from which it follows that the radiation loss coefficient (α_{rad}) is $mT/(2\pi R_{\mathrm{eff}})$ as shown in (20) at the bottom of the page where λ_o is the free-space wavelength. The results for ring waveguides with various diameters and a fixed width and thickness are shown in Fig. 15. Note that the bending radiation loss is less than 1% for diameters greater than 1 μm, but increases exponentially below that. If the waveguide thickness is decreased, the radiation loss will be larger because, first, n_v is smaller, lowering the tunneling barrier, and second, the increased diffraction effect brings the external high-index region closer to the edge of the waveguide, thereby increasing the tunneling probability.

E. Substrate Leakage Loss

Energy in a waveguide can be lost not only laterally but also vertically into the substrate. For a Type I waveguide,

the waveguide core is typically separated from the substrate by a buffer layer of thickness t_2, as shown in Fig. 2(a). A significant amount of signal attenuation in a waveguide can occur owing to leakage to the substrate if the effective index of the waveguide is below the bulk index of the substrate. Hence, the design of the buffer layer thickness is important for minimizing this leakage. A tradeoff is usually necessary between a thick buffer to minimize the leakage loss and a thin buffer to reduce the etching depth.

The leakage loss (α_L) to the substrate is very similar to the radiation loss of a curved waveguide, and can be calculated in exactly the same way using the tunneling picture. For the case where the buffer layer is etched only partially through, diffraction from the mesa into the unetched buffer can also be considered in a similar way. In the case of vertical leakage the TM polarization is expected to experience greater leakage loss due to the larger extent of the electric field in the vertical direction. (For similar reason, the TE modes will suffer greater lateral leakage loss.) A narrow waveguide is also expected to have a larger substrate leakage loss because its effective index is lower. In Fig. 16(a), α_L is calculated as a function of buffer thickness for a 0.5-μm wide waveguide with a fixed core thickness of 0.5 μm. Note that a fairly thick buffer ($t_2 > 1$ μm) is required for reasonably small leakage loss. The index contrast ($n_1 - n_c$) should be increased if a smaller

$$\alpha_{\mathrm{rad}} = \frac{n_v}{\lambda_o}\exp\left(-2\int_{u_2}^{u_o} \sqrt{k_v^2 - \left(k_2^2 - k_z^2(u)\right)\exp(2u/R_{\mathrm{eff}})}\,du\right) \qquad (20)$$
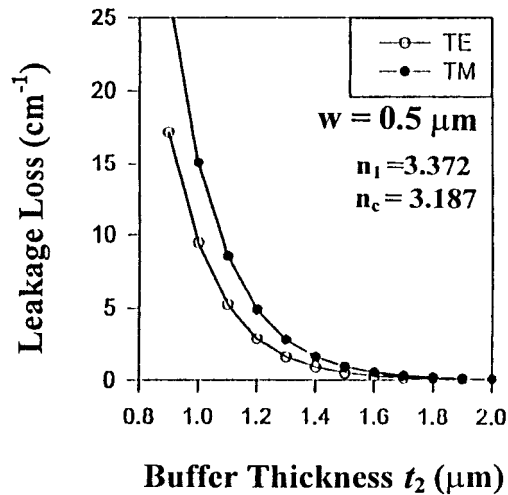
(a)
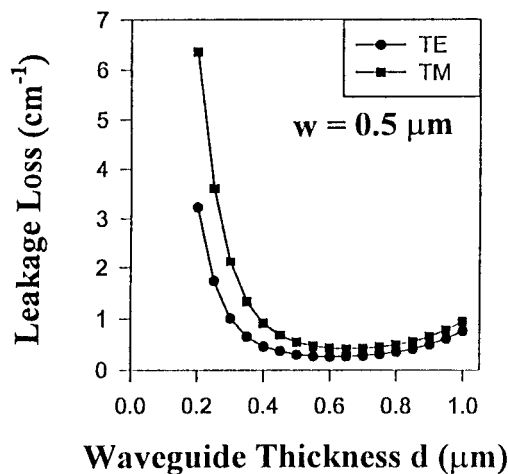
(b)

Fig. 16. (a) Substrate leakage loss as a function of the buffer thickness (t_2) for TE and TM modes. (b) Substrate leakage loss as a function of waveguide thickness, subject to the constraint that $d + t_2 = 2$ μm. A broad minimum occurs around $d = 0.6$ μm.

buffer thickness is desired. In cases where one is constrained to a fixed etching depth, the core and buffer thicknesses are not independent, and should be optimized together to yield the minimum leakage loss. As an example, Fig. 16(b) gives the leakage loss as a function of the waveguide thickness (d) under the constraint $d + t_2 = 2$ μm. A broad minimum occurs around $d = 0.6$ μm. For very thin waveguides, the leakage loss increases because of the weak confinement.

F. Vertical Resonant Coupling

The lateral coupling geometries discussed in Section III-B suffer from several disadvantages. First, in terms of fabrication, the small gap width is difficult to control. Secondly, without phase matching, the coupling length is very short. To overcome these difficulties, a novel alternative is to use the vertical coupling geometry, as shown schematically in Fig. 17. This is basically a stack structure in which two identical waveguide layers are grown epitaxially one on top of another. The epiwafer is processed in such a way that the lower
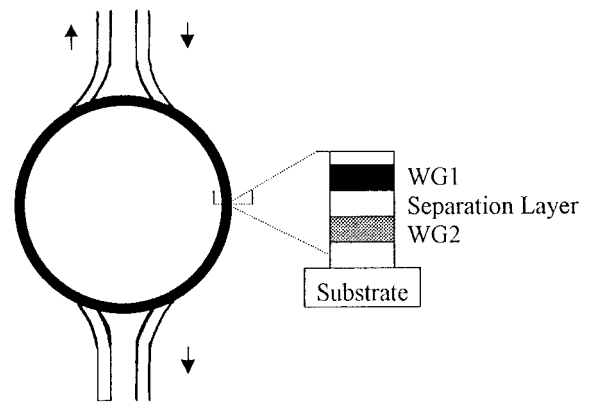

Fig. 17. Schematic of the vertical coupling geometry, showing the vertical stack structure with the ring waveguide (WG1) sitting atop the lower coupling waveguides (WG2). The separation layer determines the coupling coefficient.

waveguide is the coupling waveguide, and the material outside the ring waveguide area is etched away to leave only the input and output waveguides. The deep etching required to form such a vertical structure with low loss is not difficult as there are no small gaps to worry about. In this structure, the coupling between the waveguides is in the vertical direction. The coupling mechanism is similar to substrate leakage loss discussed in the previous section, except the coupling is phase-matched. The main advantage is that the coupling coefficient can be controlled accurately during the epitaxial growth process as it is determined primarily by the thickness of the separation layer, independent of surface scattering or edge diffraction. Since there is no phase mismatch due to path difference, the interaction length is the maximum possible. Furthermore, it is relatively easy to make electrical contact to such a device. Direct electrooptic modulation of the coupling coefficient can be achieved by doping the upper waveguide p-type, the lower waveguide n-type, and the separation layer undoped, and applying an electric field across the undoped separation layer [18]. Alternatively, if electro-optic modulation of the resonance frequency is desired, then the ring waveguide should be undoped and the electric field is applied across it. Despite these advantages, however, a major difficulty with this structure is its integrability with other devices. Further investigation of the vertical coupling structure will be given elsewhere.

IV. SUMMARY

In summary, we have discussed the design of a number of important parameters, including the resonance wavelength, the effective ring radius (R_{eff}), the coupling factor (P_c), the bending radiation loss (α_{rad}) and the substrate leakage loss (α_L), all of which are important to the operation of a waveguide-coupled microring resonator. As an example, consider the resonator *finesse* F (the ratio of FSR to the bandwidth) or the Q factor (the ratio of the absolute frequency to the bandwidth). These two parameters are both important when one is interested in both the FSR and the bandwidth. They are related by

$$\frac{Q}{F} = \frac{v_m}{\Delta v_{\text{FSR}}} = \frac{\lambda_m}{\Delta \lambda_{\text{FSR}}} = \frac{\lambda_m}{\lambda_m - \lambda_{m+1}} \cong m \qquad (21)$$
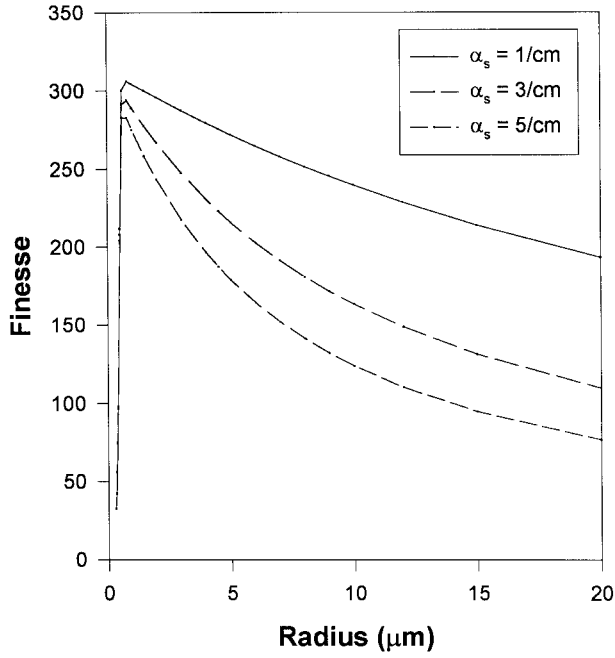
(a)
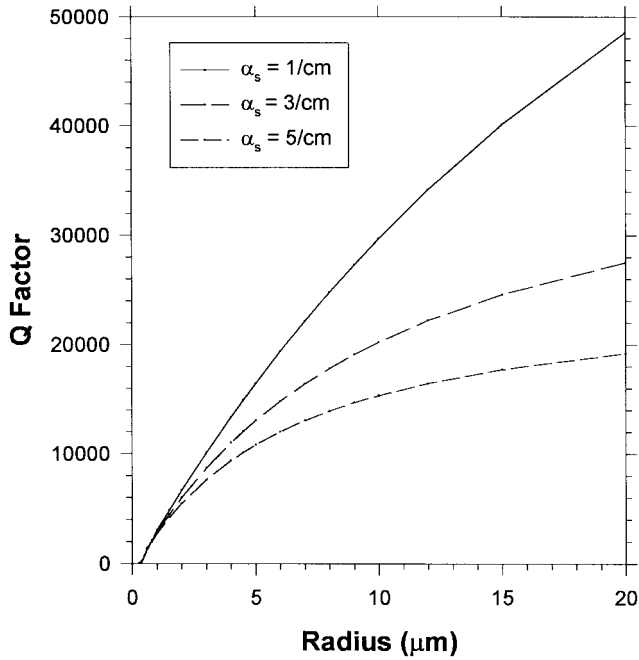
(b)

Fig. 18. (a) The finesse, and (b) the Q factor, of the microring resonator as a function of the ring radius for varying scattering loss coefficients, assuming a coupling factor of 1%. A peak in finesse occurs at the optimal radius of about 1 μm.

Using this relation, the Q factor may be written in a form that shows explicitly its dependence on all the parameters discussed above

$$Q \cong \frac{2\pi n_v R_{\text{eff}}}{\lambda_m}$$

$$\cdot \frac{\pi(r_1 r_2)^{1/2} \exp[-(\alpha_s + \alpha_{\text{rad}} + \alpha_L + \cdots)\pi R_{\text{eff}}/2]}{1 - (r_1 r_2)\exp[-(\alpha_s + \alpha_{\text{rad}} + \alpha_L + \cdots)\pi R_{\text{eff}}]}$$
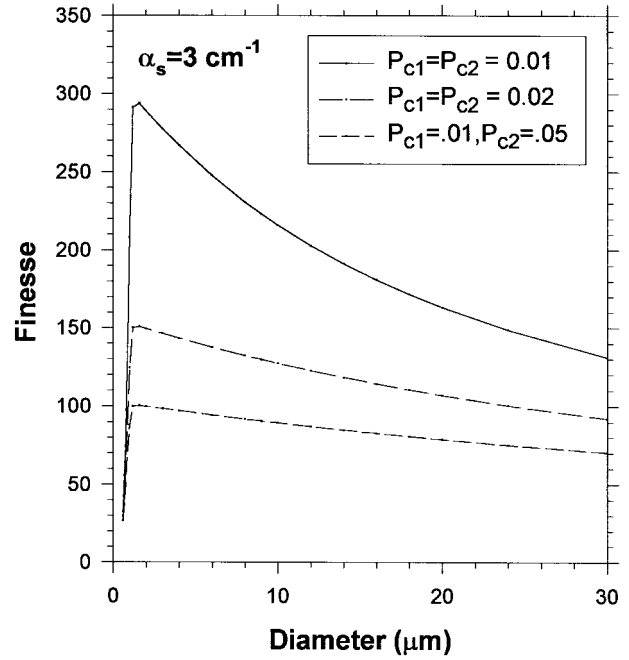
(22)

Fig. 19. The finesse of the microring resonator as a function of diameter, as the coupling factors P_{c1} and P_{c2} are varied.

where r_1 and r_2 are the reflectivities, given by $(1 - P_c)^{1/2} \equiv \cos(K_{1,2}l)$ at each waveguide-to-ring coupling point ($K_{1,2}$ are the coupling coefficients at these points). The loss terms in the exponent may include other losses such as absorption loss. α_s, the surface scattering loss in the cavity, is not considered in our model but may yet be the dominant source of loss. Fig. 18 shows both the finesse and the Q for a case of fixed $P_c = 0.01$ and varying scattering loss coefficient, $\alpha_s = 1, 3$, and 5 cm^{-1}. In each case the finesse shows a maximum "turning point" at an optimal diameter of about 2 μm. The finesse decreases for larger diameters because of increasing scattering loss, and decreases for smaller diameters because of increasing radiative bending loss. On the other hand, Q shows no such turning point in the range shown because the factor m in (22) is a monotonically increasing function of the ring diameter at a fixed wavelength. The maximum finesse at the turning point is limited by the 1-% waveguide-to-cavity coupling. If there was zero coupling and the scattering loss was also zero, then the finesse would increase indefinitely with the ring radius. On the other hand, an increase in P_c or an introduction of unbalanced P_c (i.e., K_1 not equal to K_2) will decrease the finesse, as shown in Fig. 19. The control of P_c, via accurate control of the gap size, can be achieved by nanofabrication technology as has been demonstrated for both GaAs and InP materials [4]. With the gap-enhancing designs proposed above, this control may be more reliably achieved. On the other hand, a good way to switch the resonator off is to electrooptically unbalance it so that the input coupling is different from the output coupling, analogous to the transmission of a Fabry–Perot resonator where front and back mirrors are not identical.

The conformal transformation method at the core of our model gives a good physical picture of the guiding and radiation mechanism in the microring cavity. Much of the

physics can be derived by analogy with quantum wells and tunneling through potential barriers. Based on this physical picture, we have developed a novel approach for significantly increasing the coupling length, and hence the coupling gap size, by using a phase-matched parallel waveguide having a different width than the ring waveguide. An alternative vertical coupling structure is also proposed in which the control of the coupling coefficient is built into the material growth process. The resonant coupling between two waveguides with different widths has an appropriate analogy with the resonant coupling between two quantum wells with different well widths, which can be achieved by applying an appropriate uniform electric field across the wells. Mathematically, the similarity arises because curving the waveguides has the same effect on (4) (within our linear approximation) as the presence of a uniform electric field does on the Schrodinger equation for a quantum well [14].

In summary, we have discussed an approximate model for solving the effective indexes and the eigenmodes of a micro-ring waveguide with a small radius of curvature and a large lateral index contrast. The model takes into account some 3-D effects such as waveguide dispersion and edge diffraction. The resonance frequencies and the FSR calculated with this model agree well with the FDTD method. Once the ring mode profile and the effective index are known, the coupling coefficient and its dependence on gap size can be obtained readily. The model provides physical insight and design guidance useful for first-cut optimal designs of waveguide-coupled microring resonators before tedious laboratory fabrications are carried out.

REFERENCES

[1] K. Oda, S. Suzuki, H. Takahashi, and T. Toba, "An optical FDM distribution experiment using a high finesse waveguide-type double ring resonaotr," *IEEE Photon. Technol. Lett.*, vol. 6, pp. 1031–1034, Aug. 1994.
[2] R. Orta, P. Savi, R. Tascone, and D. Trinchero, "Synthesis of multiple-ring-resonator filters for optical systems," *IEEE Photon. Technol. Lett.*, vol. 7, pp. 1447–1449, Dec. 1995.
[3] S. Suzuki, K. Oda, and Y. Hibino, "Integrated-optic, double-ring resonators with a wide free spectral range of 100 GHz," *J. Lightwave Technol.*, vol. 13, pp. 1766–1771, Aug. 1995.
[4] D. Rafizadeh, J. P. Zhang, S. C. Hagness, A. Taflove, R. C. Tiberio, K. A. Stair, and S. T. Ho, "Waveguide-coupled AlGaAs/GaAs microcavity ring and disk resonators with high finesse and 21.6-nm free spectral range," *Opt. Lett.*, vol. 22, pp. 1244–1246, Aug. 1997.
[5] S. C. Hagness, D. Rafizadeh, S. T. Ho, and T. Taflove, "FDTD microcavity simulations: Nanoscale waveguide-coupled single-mode ring and whispering-gallery-mode disk resonators," *J. Lightwave Technol.*, vol. 15, pp. 2154–2165, Nov. 1997.
[6] B. Little, G. S. T. Chi, H. Haus, J. Foresi, and J. P. Laine, "Micro-ring resonator channel dropping filters," *J. Lightwave Technol.*, vol. 15, p. 998, 1997.
[7] M. K. Chin, D. Y. Chu, and S. T. Ho, "Estimation of spontaneous emission factor for microdisk lasers via the approximation of whispering gallery modes," *J. Appl. Phys.*, vol. 75, pp. 3302–3307, Apr. 1994.
[8] H. Kogelnik, "Theory of optical waveguides," in *Guided Wave Optoelectronics*, T. Tamir, Ed. New York: Springer-Verlag, 1988, pp. 69–74.
[9] The multi-grid finite difference solution was performed with *Selene Pro* from BBV Software, Enschede, The Netherlands.
[10] M. Heiblum and J. H. Harris, "Analysis of curved optical waveguides by conformal transformation," *IEEE J. Quant. Electron.*, vol. 48, pp. 2071–2012, Sept. 1969.
[11] D. R. Rowland and J. D. Love, "Evanescent wave coupling of whispering gallery modes of a dielectric cylinder," *Inst. Elect. Eng. Proc.—J.*, vol. 140, pp. 177–188, June 1993.
[12] D. Rafizadeh and S. T. Ho, "Numerical analysis of vectorial wave propagation in waveguides with arbitrary refractive index profiles," *Opt. Commun.*, vol. 141, pp. 17–20, Aug. 1997.
[13] S. L. McCall, A. F. J. Levi, R. E. Slusher, S. J. Pearton, and R. A. Logan, "Whispering-gallery mode microdisk lasers," *Appl. Phys. Lett.*, vol. 60, p. 289, 1992.
[14] M. K. Chin, "Modeling of InGaAs/InAlAs coupled double quantum wells," *J. Appl. Phys.*, vol. 76, pp. 518–523, 1994.
[15] I. C. Goyal, R. L. Gallawa, and A. K. Ghatak, "Bent planar waveguides and whispering gallery modes: A new method of analysis," *J. Lightwave Technol.*, vol. 8, pp. 768–773, 1990.
[16] A. Yariv and P. Yeh, *Optical Waves in Crystals*. New York: Wiley, 1984, p. 183.
[17] R. L. Liboff, *Introductory Quantum Mechanics*. New York: Holden-Day, pp. 248–249, 1980.
[18] M. K. Chin, "Design considerations for vertical directional couplers," *J. Lightwave Technol.*, vol. 11, pp. 1331–1336, 1993.

M. K. Chin (M'92) received the B.S. degree from the Massachusetts Institute of Technology, Cambridge, in 1986 and the Ph.D. degree from the University of California, San Diego, in 1992. His Ph.D. work was on the design and fabrication optimization of quantum-well electroabsorption modulators.

From September 1992 to May 1993, and from March 1997 to June 1998, he was a Research Associate at Northwestern University, Evanston, IL, where he worked with Prof. S. T. Ho on microcavity devices and nanofabrications. During the interim, he was an Assistant Professor at the Nanyang Technological University, Singapore, where he founded the first Photonics Laboratory and did research in soliton communications and diode-pumped solid-state lasers. He is now Manager for Technology Development at the United States Integrated Optics, Inc., Evanston, IL, a high-tech start-up.

S. T. Ho (S'83–M'89) received the B.S., M.S., and Ph.D. degrees in electrical engineering from the Massachusetts Institute of Technology, Cambridge, in 1984 and 1989, respectively.

From 1989 to 1992, he was a Member of Technical Staff at AT&T Bell Laboratories, Murray Hill, NJ. Since 1991, he has been a Faculty Member in the Department of Electrical and Computer Engineering at Northwestern University, Evanston, IL. His research areas include microcavity lasers, quantum phenomena in low-dimensional photonic structures, nanofabrication, ultrafast nonlinear optical phenomena, optical communications, and quantum optics.

Dr. Ho is a member of Phi Beta Kappa, Tau Beta Pi, Sigma Pi Sigma, and Sigma Xi.